ADVANCED
FUNCTIONAL
MATERIALS

Supporting Information

for *Adv. Funct. Mater.*, DOI: 10.1002/adfm.202001619

Li-CO_2 Batteries Efficiently Working at Ultra-Low Temperatures

Jiaxin Li, Lie Wang, Yang Zhao, Shangyu Li, Xuemei Fu, Bingjie Wang, and Huisheng Peng**

Supporting Information

Calculation of the electrolyte evaporation rate

Li-CO_2 battery is a semi-open system in which the electrolyte experiences an inevitable continuous volatilization through its porous cathode. It was ever reported that the evaporation rate of solvent could be calculated according to Donald Mackay's work,[1,2]

$\boldsymbol{E}_{mass}\left(\mu g \cdot m^{-2} \cdot h^{-1}\right) = 1464 \times \boldsymbol{P}(Pa) \times \boldsymbol{M}(g \cdot mol^{-1})$, where $\boldsymbol{P}$ and $\boldsymbol{M}$ represent the vapor pressure and the relative molecular mass of electrolyte. It is noted this equation is only applied to the liquid surfaces that are not covered by the underlying solid substrate as occurs in the standard evaporation rate test and static liquid pools. For a real battery, the electrolyte is usually contained in separators and covered by the cathode and battery mold, so a realistic evaporation rate should be smaller than the above calculation results. In addition, the vapor pressure of a solvent also depends on the ambient temperature, which is described by the Antoine equation,[3,4] $log\boldsymbol{P}(kPa) = \boldsymbol{A} - \frac{\boldsymbol{B}}{\boldsymbol{T}(\,^{o}C)+\boldsymbol{C}}$,

where $\boldsymbol{P}$ is expressed in kPa, $\boldsymbol{T}$ in ^{o}C, and $\boldsymbol{A}$, $\boldsymbol{B}$, and $\boldsymbol{C}$ are changeable parameters associated with the type of molecules and temperature range. Although neither the accurate vapor pressures nor the specific parameters in Antoine equation for DOL at low temperatures were found in literature so far, some approximate calculation and further qualitative deductions still could be obtained from the existing data available.

One the one hand, the evaporation rate of DOL-based electrolyte at near 0 ^{o}C could be estimated and thus the impact of Parafilm as the cathode protective layer was further confirmed. The lowest measurement temperature of DOL vapor pressure reported in the literature was found to be 280.46 K (7.31 °C, 5,422 Pa),[4] which was used to approximate the DOL vapor pressure at about 0 °C. Based on Raoult's law, which says that the vapor pressure of a solvent in dilute solution is proportional to the mole fraction of the solvent in the solution at a certain temperature,[5] the partial vapor pressure of DOL solvent in electrolyte is calculated as

$\boldsymbol{P}_{electrolyte} = \boldsymbol{P}_{solvent} \times \frac{\boldsymbol{n}_{solvent}}{\boldsymbol{n}_{solvent}+\boldsymbol{n}_{salt}}$, where $\boldsymbol{n}$ is the molar amount and expressed in mol. The deviation of real electrolyte from an ideal solution is not considered here. For 10 mL electrolyte of 1.0 M LiTFSI in DOL, the molar amount of DOL is obtained as

$$\boldsymbol{n}_{solvent} = \frac{106.5\times10\ (g)}{74.08\ (g\cdot mol^{-1}\ )} = 14.38\ mol.$$

Then the evaporation rate of DOL from electrolyte is figured out by the following process,

$$\boldsymbol{P}_{electrolyte} \approx 5422 \times \frac{14.38}{14.38+1} = 5069\ Pa,$$

$$\boldsymbol{E}_{electrolyte}\ \left(\mu g \cdot m^{-2} \cdot h^{-1}\right) = 1464 \times 5069\ (Pa) \times 74.08\ \left(g \cdot mol^{-1}\right) \times 10^{-3}$$

$$= 549749\ \left(mg \cdot m^{-2} \cdot h^{-1}\right),$$

$$\boldsymbol{S} = \pi \times 4 \times 4\ (mm^2) \times 10^{-6} = 5.03 \times 10^{-5}\ (m^2),$$

$$\boldsymbol{V} = E \times S = 549749 \times 5.03 \times 10^{-5} = 27.65\ (mg \cdot h^{-1}),$$

$$\boldsymbol{m} \approx 106.5 \left(g \cdot ml^{-1}\right) \times 200 \times 10^{-3} \times 1000 = 21.3\ (mg),$$

$$\boldsymbol{t} = \frac{21.3}{27.65} h = 0.77\ h.$$

Where $\boldsymbol{P}$, $\boldsymbol{E}$, $\boldsymbol{S}$, $\boldsymbol{V}$, $\boldsymbol{m}$, $\boldsymbol{t}$ are the partial pressure of DOL in electrolyte, the evaporation rate of DOL from electrolyte, the area of the open hole on the Swagelok-type battery (namely the exposure area of electrolyte), the unit rate of electrolyte, the mass of 200 μL DOL-based electrolyte and a theoretical evaporation time, respectively. A theoretical complete evaporation time of DOL-based electrolyte at 7.31 ^{o}C was approximated even less 1 h as the below process shown. But in fact, due to the barrier of the separator, porous cathode and foam Ni, the actual exposure area of DOL should be much smaller than the calculated area of open hole on the Swagelok-type battery. In addition, due to the descending vapor pressure value at 0 ^{o}C, a realistic time for complete solvent evaporation at 0 °C will be longer than the above calculation result.

However, obviously, the separator and porous cathode only have limited effects on inhibiting the electrolyte evaporation. At a real battery, the rapid electrolyte evaporation would inevitably result in a decreasing conductivity at relatively high temperatures. Here, the Parafilm was skillfully used as a protective layer to inhibit the evaporation of electrolyte through porous cathode. As shown in Figure S9, the operating time of battery without Parafilm sealing was much shorter than that with

Parafilm sealing. But actually the Parafilm could only slow down the rate of solvent evaporation to some degree rather than completely stop the process. During long-term operation, the electrolyte evaporation still should be viewed as a factor leading to the deterioration of battery performance at higher temperatures.

On the other hand, it is easy to speculate the vapor pressure of solvent will decrease rapidly with temperature falling from 0 ^{o}C to -60 ^{o}C. It has been reported that the vapor pressure of DOL reduced by nearly five times when the temperature decreased from 75 to 30 ^{o}C.[3] The vapor pressure values of some similar cyclic ether molecules decreased by one to two orders of magnitude with a descending temperature of 60 °C.[6] Therefore, a reasonable deduction is made that there will be a similar downward degree in the vapor pressure value when temperature decreased from 0 to -60 ^{o}C. There will also be a significant decrease in the electrolyte evaporation rate accordingly. Consequently, the suppression of electrolyte evaporation at ultra-low temperatures should be regarded as a possible reason for long battery lifespan. Besides, the solubility of CO_2 in electrolyte will increase with a decrease in temperature,[7,8] and it could overcome some adverse effects of low temperature on the battery kinetics to some extent.

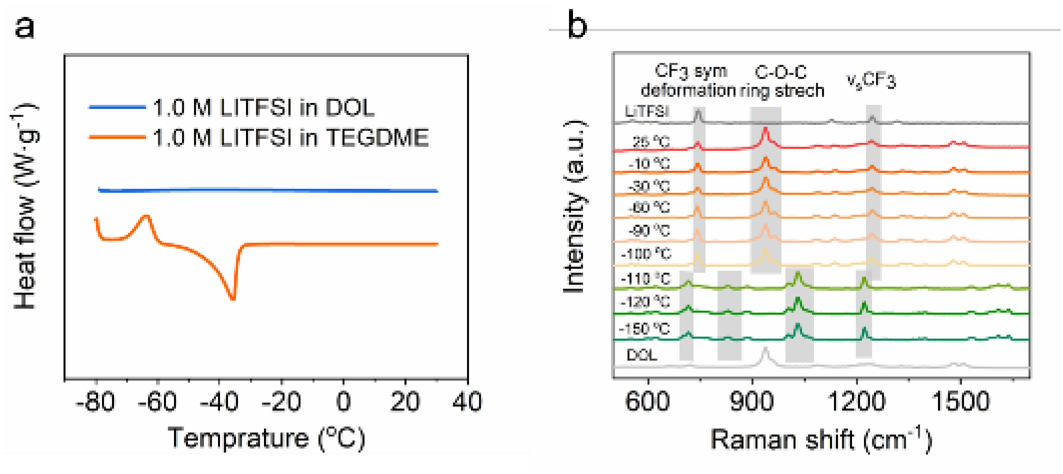

Figure S1. (**a**) Differential scanning calorimetry curves for DOL-based and TEGDME-based electrolytes. (**b**) Raman spectra for DOL-based electrolyte at different temperatures. Differential scanning calorimetry curves demonstrate that the freezing point of DOL-based electrolyte is below -80 ^{o}C, while TEGDME-based electrolyte is completely frozen at around -40 ^{o}C. The Raman characteristic peaks of C-O-C ring stretch associated with DOL molecules and CF_3 in TFSI$^-$ anions nearly remain unchanged as the temperature decreases from 25 to -100 ^{o}C, indicating that the freezing point of DOL-based electrolyte is below 100 ^{o}C and the solvated structure of Li ion in electrolyte is stable regardless of environmental temperature.

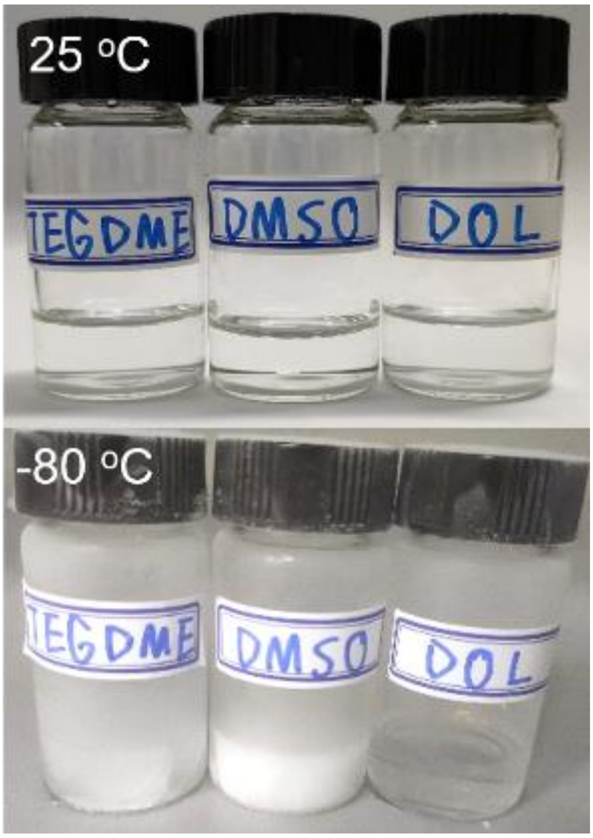

Figure S2. Photographs of 1.0 M LiTFSI in TEGDME, DMSO and DOL at 25 ^{o}C and -80 ^{o}C. While the TEGDME-based and DMSO-based electrolytes are completely frozen at -80 °C, the DOL-based electrolyte is still in the liquid state.

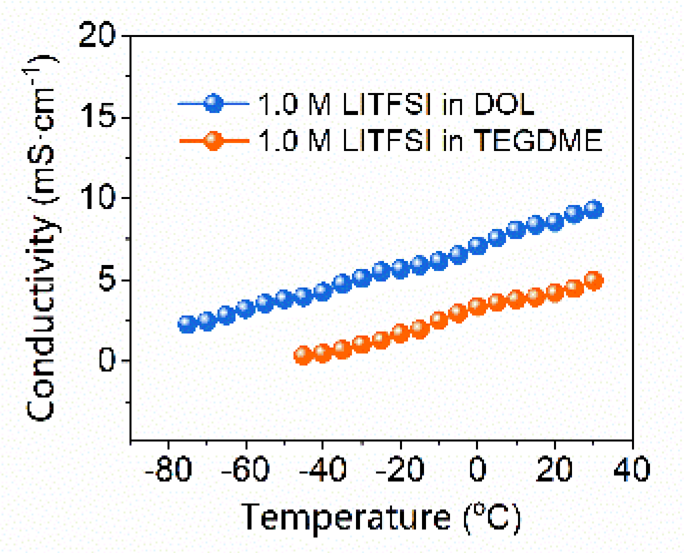

Figure S3. Comparison of ionic conductivities of DOL-based and TEGDME-based electrolytes at different temperatures.

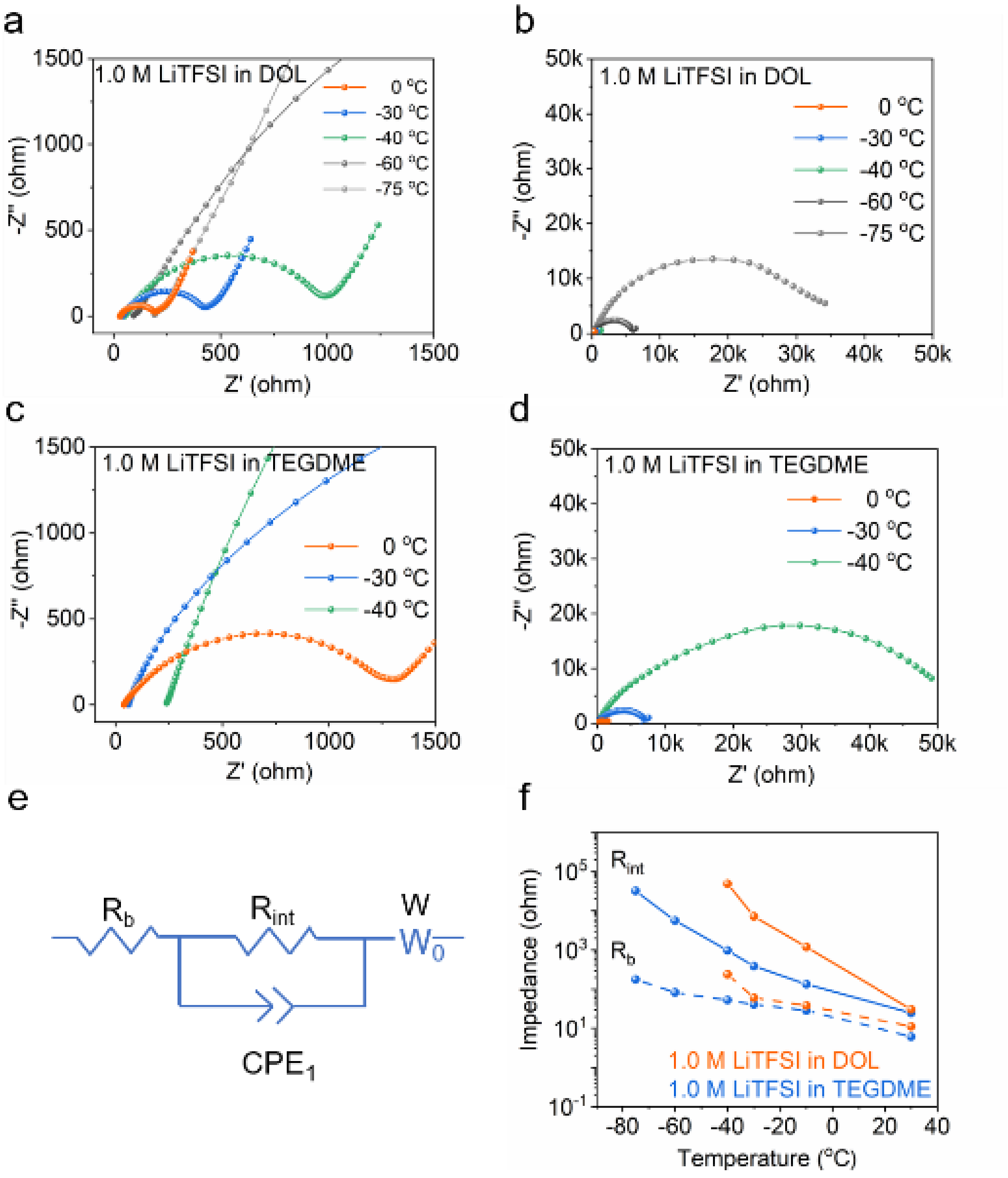

Figure S4. Electrochemical impedance spectra of Li-CO_2 batteries using the electrolytes of (**a, b**) 1.0 M LiTFSI in DOL and (**c, d**) 1.0 M LiTFSI in TEGDME at different low temperatures. (**e**) Equivalent circuit diagram of the Li-CO_2 battery. (**f**) The dependence of impedance values of DOL-based and TEGDME-based electrolytes on temperature. In the Nyquist plot, the horizontal axis intercept in the high-frequency region represents the bulk resistance (R_b), and the following semicircle is assigned to the interfacial resistance of battery (R_{int}=R_{int1}+R_{int2}).[9] It is clear that the both R_b and R_{int} of Li-CO_2 batteries using the DOL-based electrolyte are much lower than those employed regular TEGDME-based electrolyte over the temperature range shown.

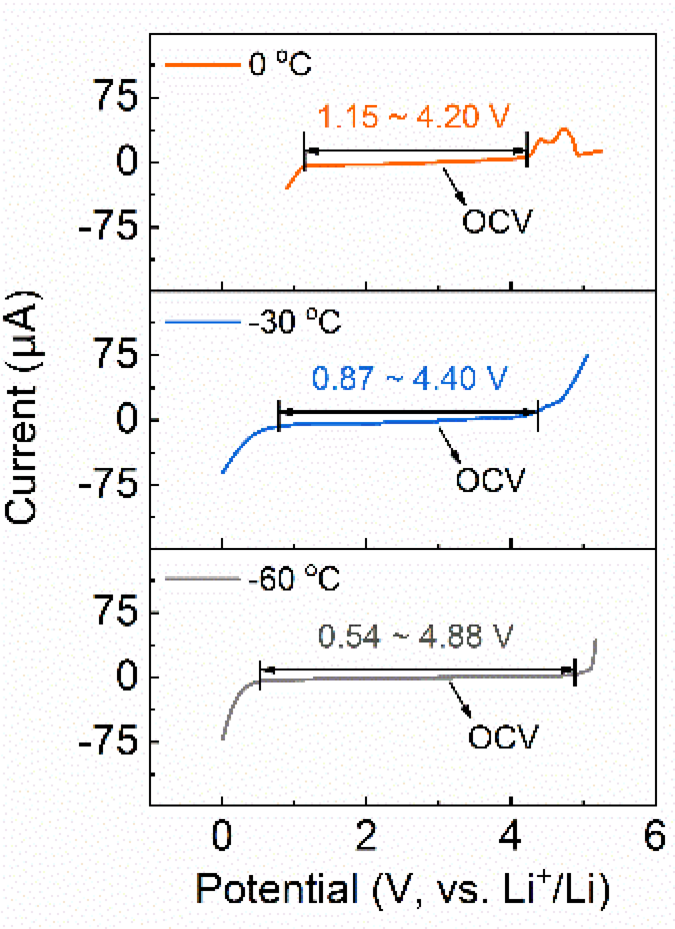

Figure S5. The stable voltage window curves of DOL-based electrolyte at 0 °C, -30 °C, and -60 °C. Note that the electrochemical stability of electrolyte is improved with the descending temperatures. Although the oxidation stability of DOL-based electrolyte is not very high at 0 °C with an decomposition voltage at around 4.2 V, it increases to approximately 4.4 V at -30 °C and 4.8 V at -60 °C. High oxidation stability at lowered temperatures makes the electrolyte be able to withstand increased battery polarization at -60 °C.

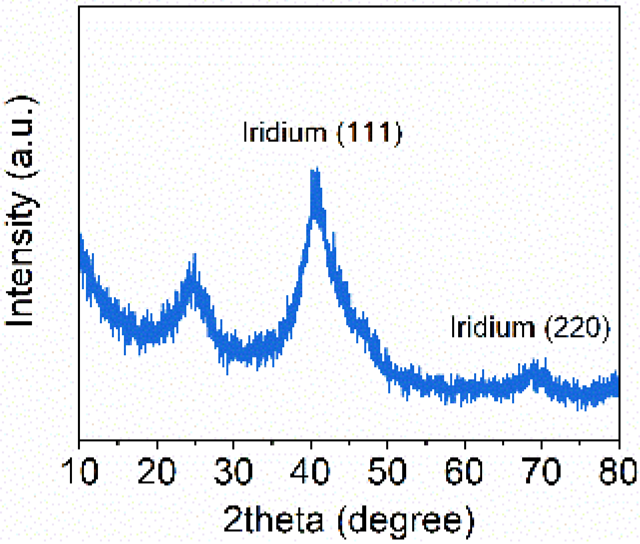

Figure S6. X-ray diffraction pattern of the iridium-carbon powder (JCPDS card No. 06–0598).

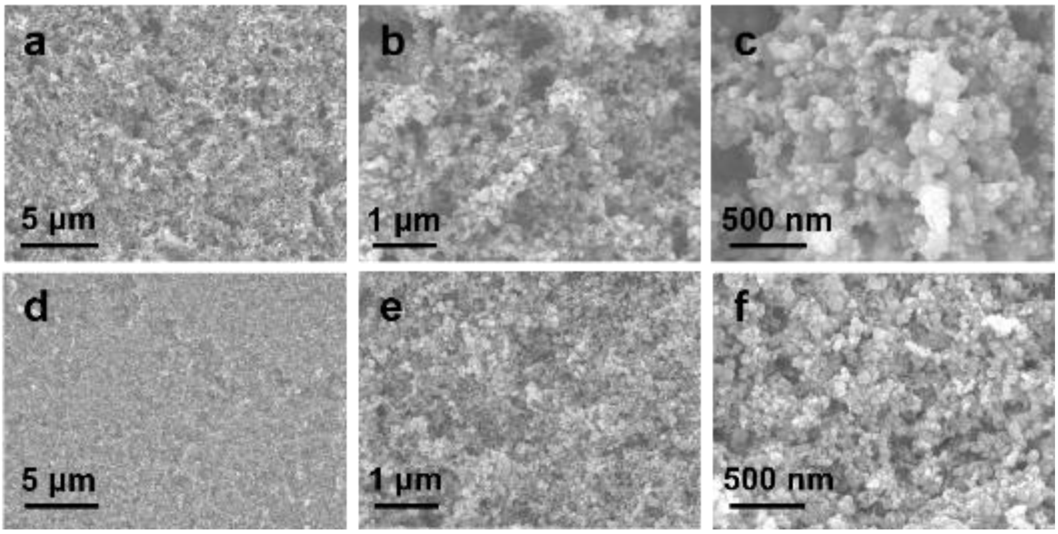

Figure S7. Scanning electron microscopy images of (**a-c**) GDL and (**d-f**) iridium-based cathode at different magnifications.

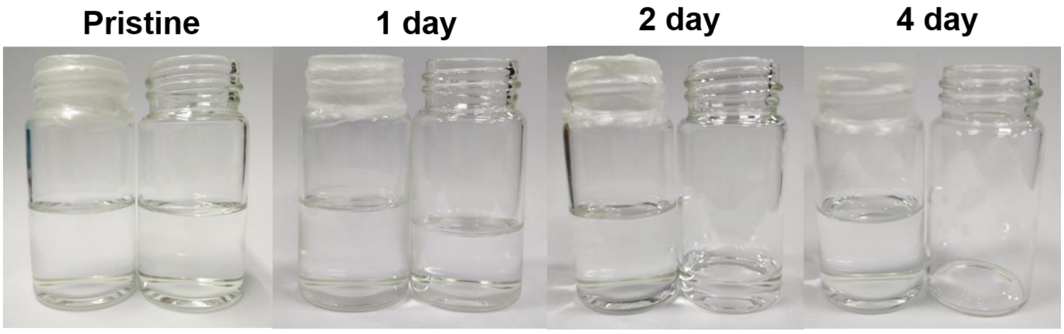

Figure S8. Comparison of the evaporation process of DOL at 0 ^{o}C with and without Parafilm sealing. DOL in left Parafilm-sealed bottle hardly evaporates over a 4-day period, while the solvent in right bottle without Parafilm sealing is completely volatile. Parafilm could effectively prevent the evaporation of DOL.

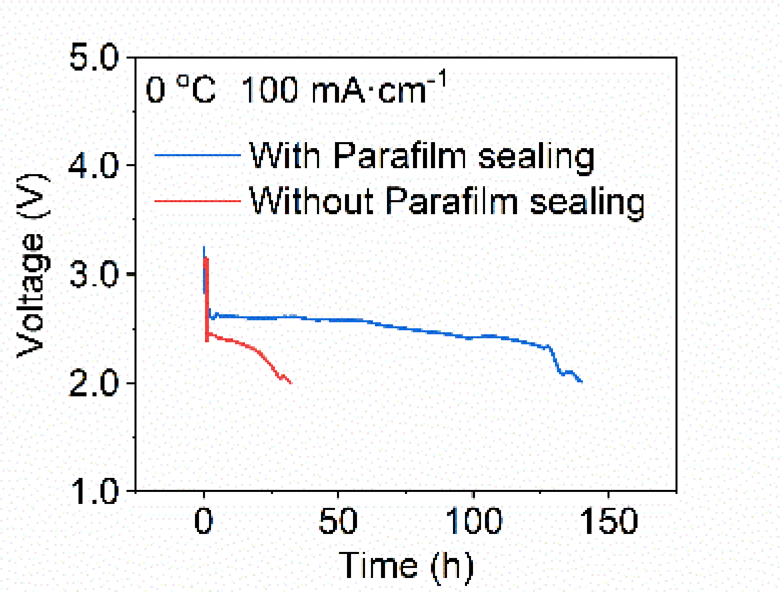

Figure S9. Discharge curves of Li-CO_2 batteries with and without Parafilm sealing at 0 ^{o}C. The operating time of Li-CO_2 battery with Parafilm as cathode protective layer is much longer than that without Parafilm sealing. Parafilm could significantly extend the battery lifespan by inhibiting the evaporation of electrolyte.

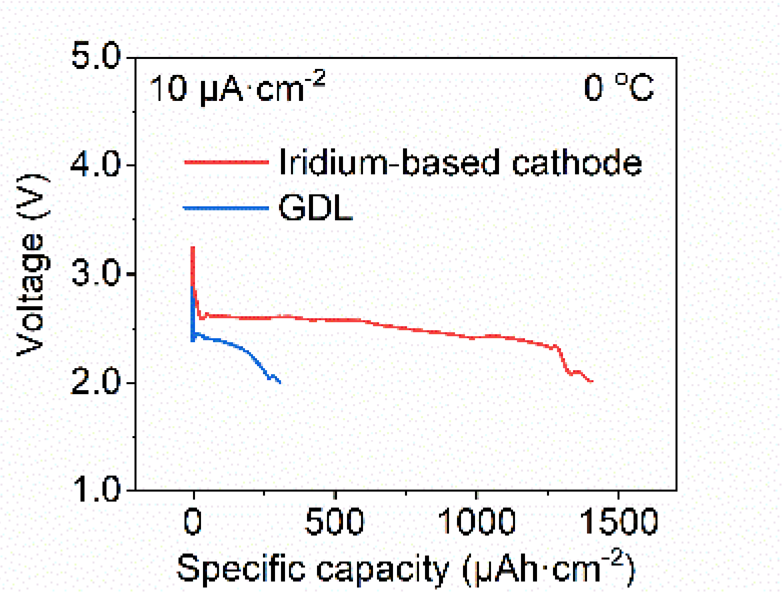

Figure S10. Discharge curves of Li-CO_2 batteries using GDL and iridium-based cathodes at 0 ^{o}C. The introduction of iridium significantly lowers discharge overpotential and extends operating time at 0 ^{o}C.

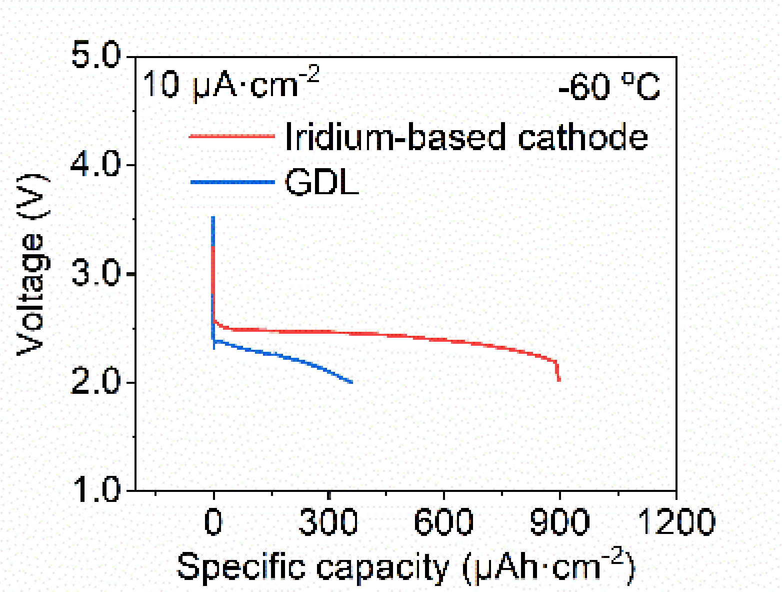

Figure S11. Discharge curves of Li-CO_2 batteries using GDL and iridium-based cathodes at -60 ^{o}C. The discharge polarization degree of Li-CO_2 battery is decreased and thus the discharge time is significantly extended after introducing the iridium catalyst at -60 ^{o}C.

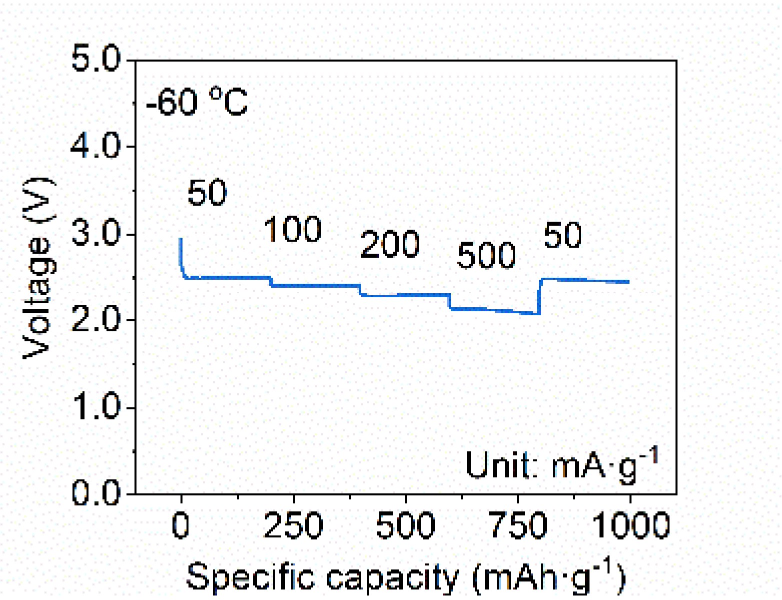

Figure S12. Rate discharge curve of Li-CO_2 battery at -60 °C.

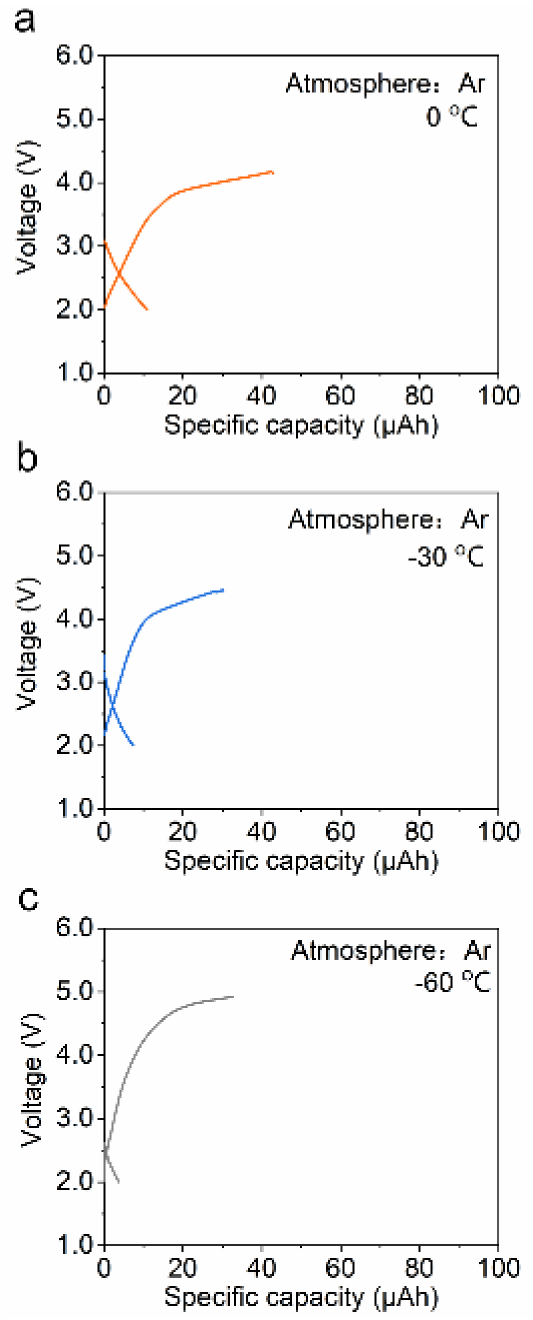

Figure S13. Discharge and charge curves in argon at (**a**) 0, (**b**) -30 and (**c**) -60 °C.

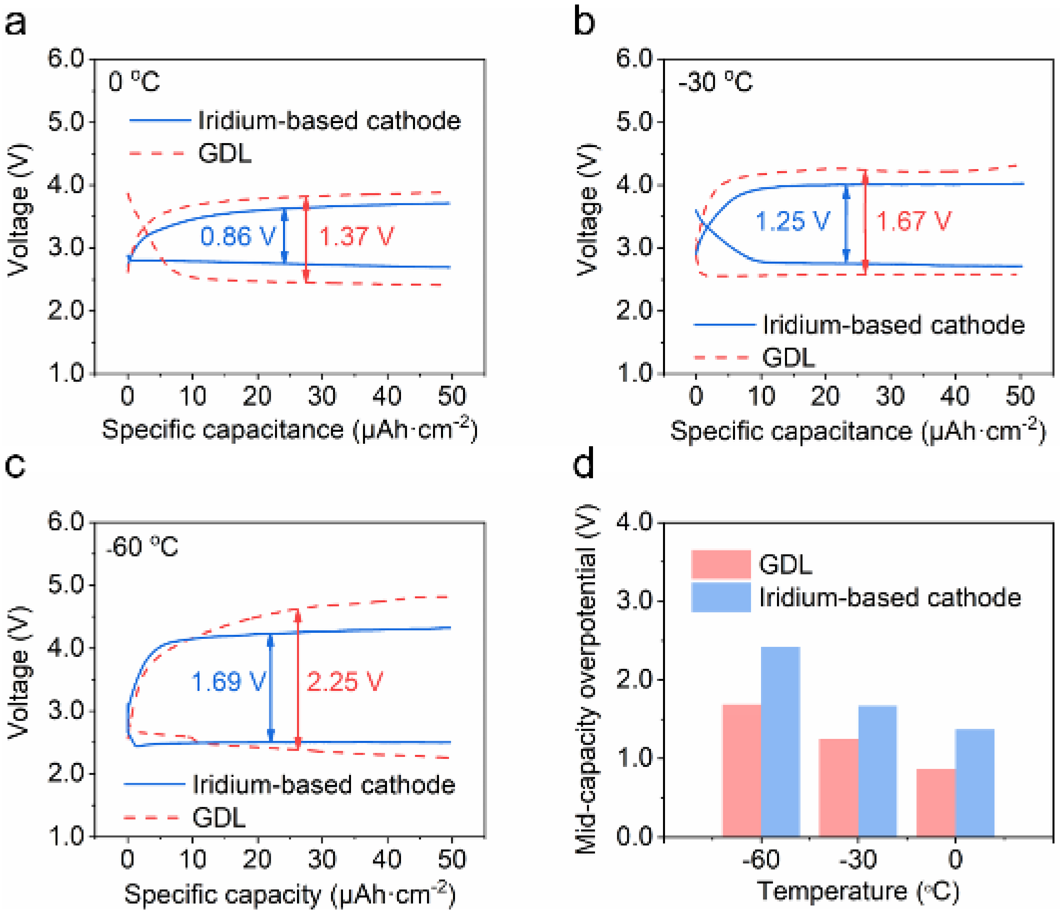

Figure S14. Discharge and charge curves at the first cycle of Li-CO_2 batteries using iridium-based and GDL cathodes at (**a**) 0, (**b**) -30, and (**c**) -60 °C. (**d**) Comparison of the mid-capacity overpotentials at the first cycle of Li-CO_2 batteries using GDL and iridium cathodes at different temperatures. It is noticeable that the introduction of iridium obviously decreases the discharge/charge overpotential of Li-CO_2 batteries at various testing temperatures.

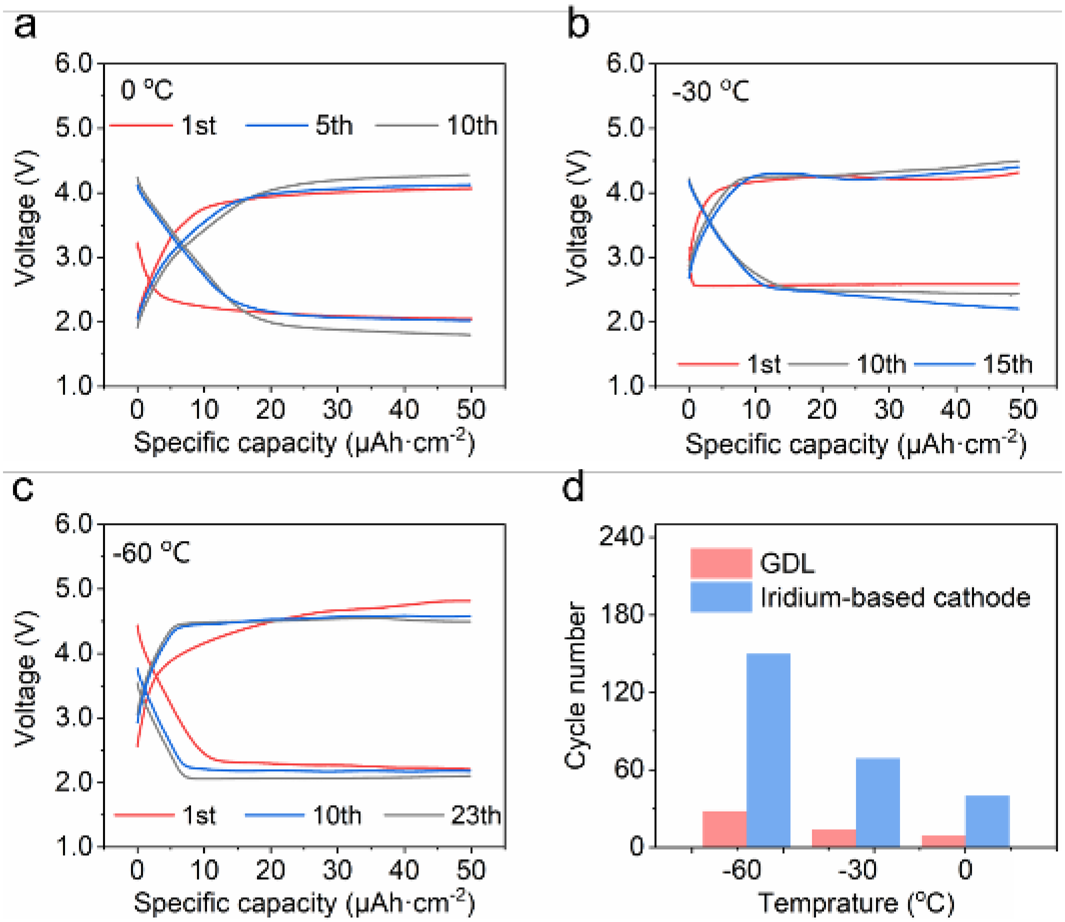

Figure S15. Selected discharge and charge curves of Li-CO_2 batteries using GDL cathodes at (**a**) 0, (**b**) -30, and (**c**) -60 ^{o}C. (**d**) Comparison of cycle number of Li-CO_2 batteries using GDL and iridium cathodes at different temperatures. It is noticeable that the introduction of iridium catalyst obviously extends the operating time of Li-CO_2 batteries at various testing temperatures.

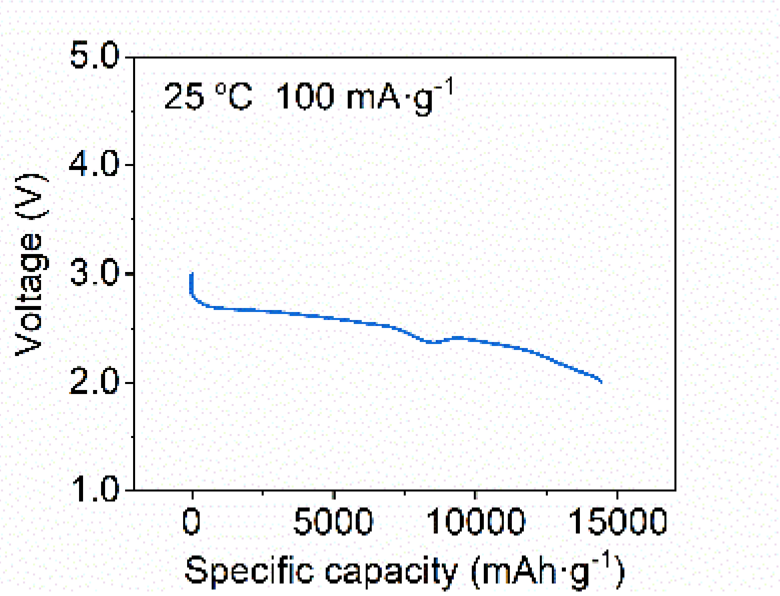

Figure S16. Discharge profile of Li-CO_2 battery with a current density of 100 mA·g^{-1} at 25 ^{o}C.

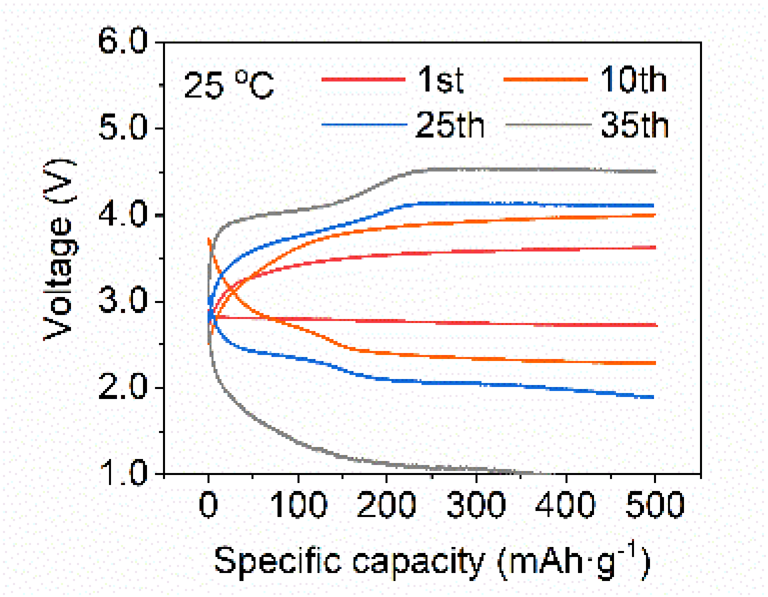

Figure S17. Selected discharge/charge curves of Li-CO_2 battery with a limited specific capacity of 500 mAh·g^{-1} and a current density of 100 mA·g^{-1} at 25 ^{o}C.

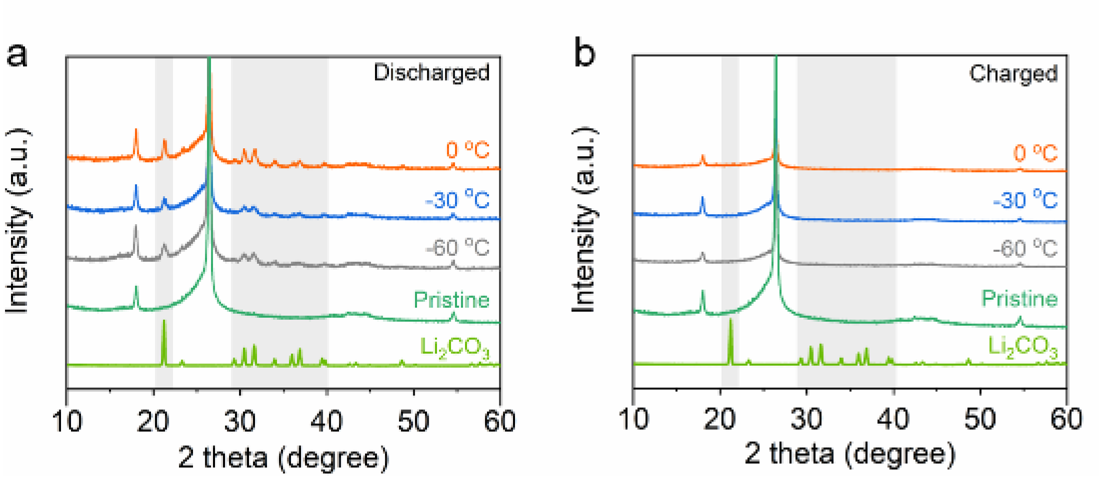

Figure S18. X-ray diffraction patterns of the iridium-based cathodes (**a**) after the initial discharge and (**b**) recharge process at different temperatures.

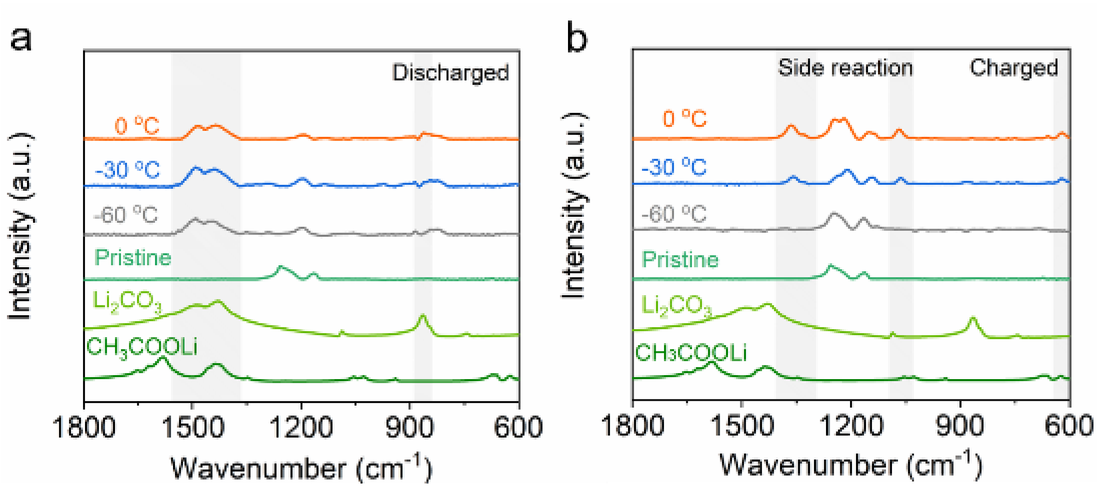

Figure S19. Fourier transform infrared spectra of the iridium-based cathodes after (**a**) initial discharge process and (**b**) recharge process at different temperatures.

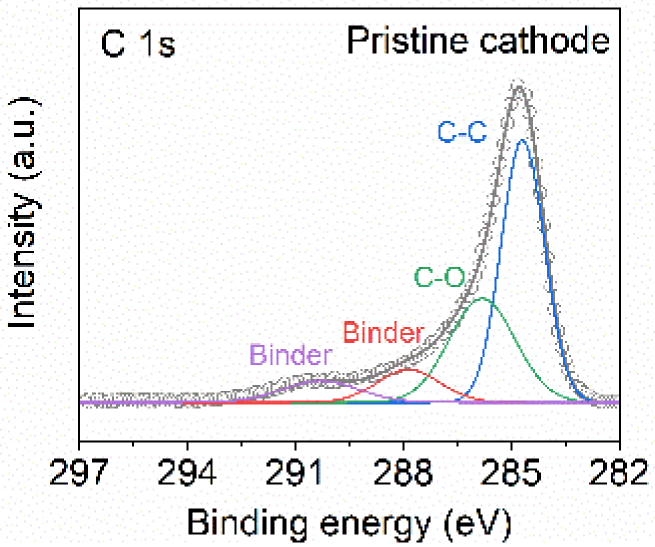

Figure S20. C 1s X-ray photoelectron spectrum for the pristine iridium-based cathode.

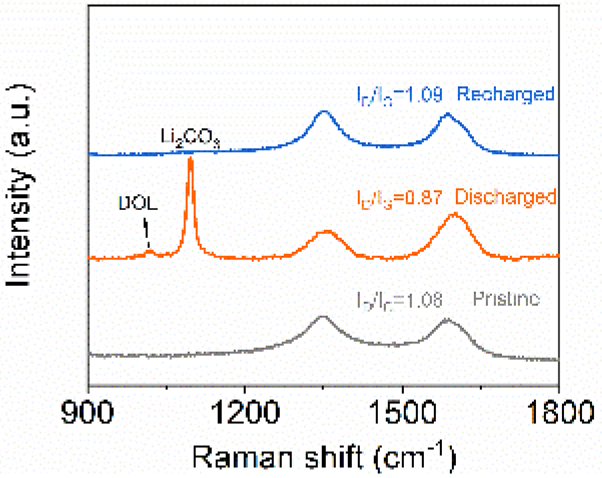

Figure S21. Raman spectra for the pristine, discharged and recharged iridium-based cathodes at -60 ^{o}C. The appearance and disappearance of Li_2CO_3 signal show the reversibility of Li-CO_2 battery at ultra-low temperatures. At the same time, it is worth noting that the changes of the intensity ratio of D-band to G-band (I_D/I_G) after discharge and recharge, which could demonstrate the formation and decomposition of carbon.

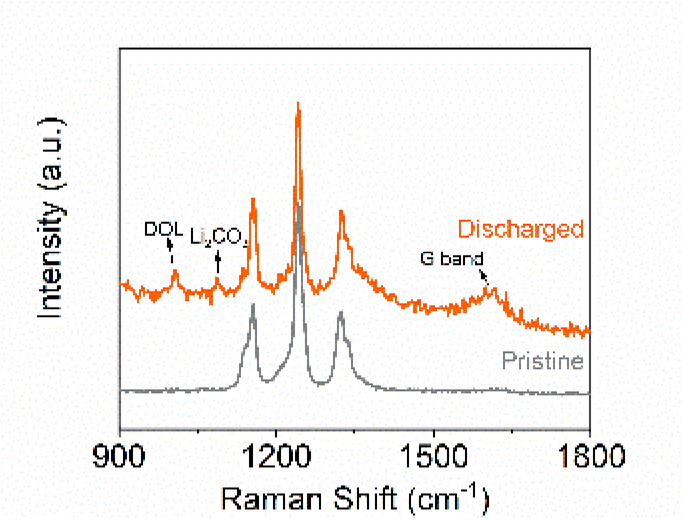

Figure S22. Raman spectra of the pristine and discharged carbon-free iridium-coated Ni foam cathodes at -60 °C. The figure shows that both Li_2CO_3 and carbon appear on the cathode as discharge products.

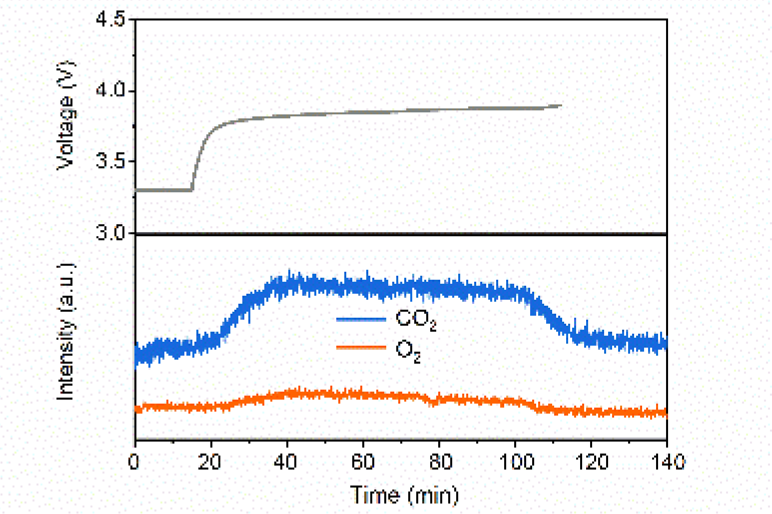

Figure S23. Differential electrochemical mass spectrometry demonstrating the evolving gases during the charge process of Li-CO$_2$ battery at a current density of 0.05 mA·cm^{-2} and the corresponding voltage curve in an ultra-low-temperature environment of approximately -70 ^{o}C, which is achieved by a dry ice bath. The evolution of CO$_2$ during charging qualitatively demonstrates the battery reversibility at ultra-low temperatures.

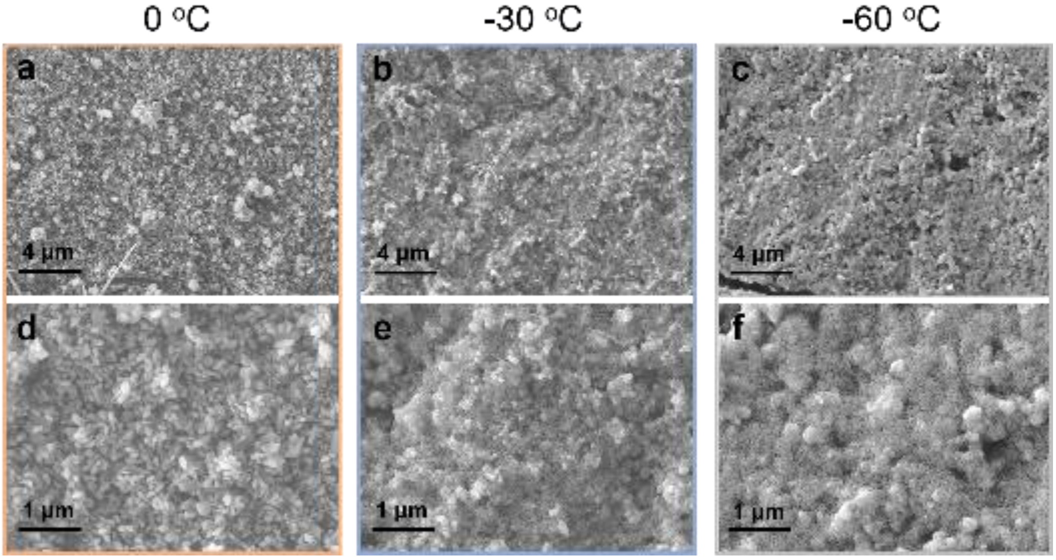

Figure S24. Scanning electron microscopy images of the iridium-based cathodes after initial discharge at (**a**, **d**) 0, (**b**, **e**) -30 and (**c**, **f**) -60 ^{o}C.

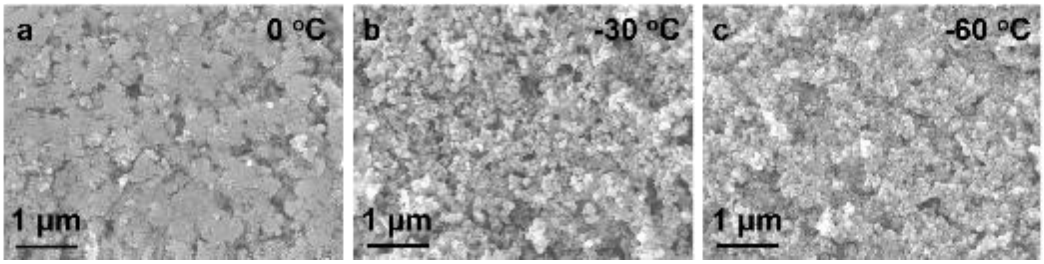

Figure S25. Scanning electron microscopy images of the iridium-based cathodes after ten cycles at (**a**) 0, (**b**) -30 and (**c**) -60 ^{o}C.

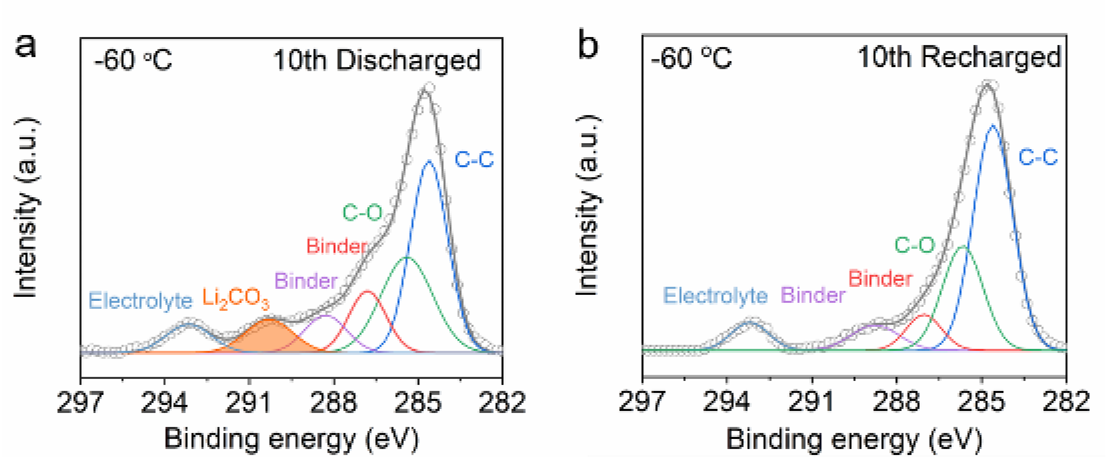

Figure S26. C 1*s* X-ray photoelectron spectra of the iridium-based cathodes after the 10th (**a**) discharge and (**b**) recharge at -60 °C.

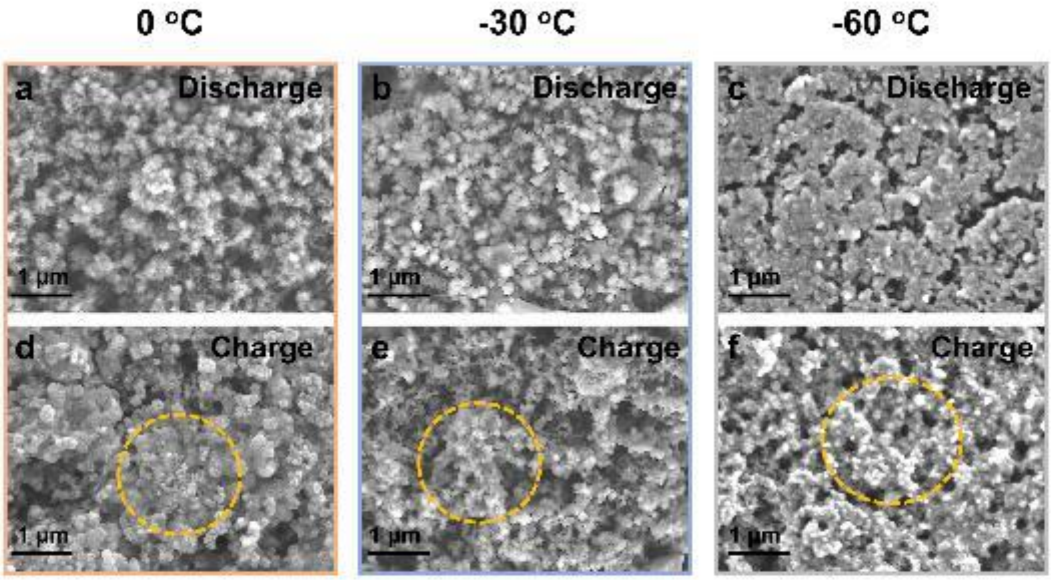

Figure S27. Scanning electron microscopy images of the discharged and charged GDL cathodes at (**a, d**) 0, (**b, e**) -30 and (**c, f**) -60 °C.

Table 1. Physical properties of some solvents ever used in aprotic metal-gas batteries.[17]

`Solvent	**Molecular formula**	**Molecular weight**	**Density ($g \cdot cm^{-3}$, 25 ^oC)**	**Freezing point (^oC)**	**Boiling point (^oC)**
Dimethyl sulfoxide (DMSO)[10]	C_2H_6OS	78.13	1.10	18.4	189
1-ethyl-3-methylimidazolium tetra-fluoroborate (EMIM-BF_4)[10]	$C_6H_{11}BF_4N_2$	197.97	1.29	11	Not available
tetraglyme[11]	$C_{10}H_{22}O_5$	222.28	1.01	-30	275-276
diglyme[12]	$C_4H_{10}O_2$	90.12	0.86	-58	82-83
1, 3-dioxolane (DOL)[13]	$C_3H_6O_2$	74.08	1.06	-95	74-75
2-methyl-tetrahydrofuran (2-MTHF)[14]	$C_5H_{10}O$	86.13	0.86	-136	78-80
2-dimethoxyethane (DME)[15]	$C_6H_{14}O_3$	134.18	0.87	-64	160
N, N-Dimethylformamide (DMF)[16]	C_3H_7NO	73.09	0.95	-61	153
N, N-Dimethylacetamide (DMA)[17]	C_4H_9NO	87.12	0.94	-20	164-166

Table S2. Comparison and summary of recent studies on low-temperature metal-gas batteries.

Battery type	Lowest Temperature	Electrolyte	Cathode	Capacity	Cyclicity	Reference
Li-CO$_2$	**-60 °C**	**LiTFSI in DOL**	**Iridium-coated GDL**	**8976 mAh·g^{-1}**	**150 cycles（100 mA·g^{-1}/500 mAh·g^{-1}）**	**This work**
Li-O$_2$	-20 °C	LiClO$_4$ in TEGDME	IrO$_2$/MnO$_2$	1037 mAh·g^{-1} (200 mA·g^{-1})	83 cycles (200 mA·g^{-1}/500 mAh·g^{-1})	Zhao et al.[18]
Li-O$_2$	-20 °C	LiClO$_4$ in DME	Carbon nanotube	17716 mAh·g^{-1} (0.1 mA·cm^{-2})	Not available	Zhang et al.[19]
Li-air	-73 °C	$Li_{1.5}Al_{0.5}Ge_{1.5}P_3O_{12}$	Engineering plasmonic air cathode	~3600 mAh g^{-1}（under Xe-lamp irradiation）	15 cycles（400 mA·g^{-1}/1000 mAh·g^{-1}）	Zhou et al.[20]
Zn-air	-20 °C	A-PAA hydrogel	Bamboo-shaped fibrous catalysts	691 mAh·g^{-1}	600 cycles（2 mA·cm^{-2}）	Chen et al.[21]

Table S3. Summary of the morphology and size of discharge products at low temperatures.

Temperature	**Morphology**	**Size**
0 ^{o}C	Flake	150-400 nm
-30 ^{o}C	Spherical particle	35-70 nm
-60 ^{o}C	Spherical particle	15-40 nm

Supporting references

[1] S. Yang, Y. Qiao, Y. Liu, Z. Cheng, H. Zhou, *Energy Environ. Sci.* **2017**, *10*, 972.

[2] D. Mackay, I. van Wesenbeeck, *Environ. Sci. Technol.* **2014**, *48*, 10259.

[3] H. S. Wu, S. I. Sandler, *J. Chem. Eng. Data* **1989**, *34*, 209.

[4] L. Lepori, E. Matteoli, P. Gianni, *J. Chem. Eng. Data* **2017**, *62*, 194.

[5] J. B. Ott, J. Boerio-Goates, In *Chemical Thermodynamics: Advanced Applications*; Ott, J. B.; Boerio-Goates, J. B. T.-C. T. A. A., Eds.; Academic Press: London, 2000; pp. 1–42.

[6] Broughton, G., *The Handbook of Solvents(Fourth Edition).*; 2007; Vol. 76.

[7] A. Henni, P. Tontiwachwuthikul, A. Chakma, *Can. J. Chem. Eng.* **2008**, *83*, 358.

[8] X. Gui, Z. Tang, W. Fei, *J. Chem. Eng. Data* **2011**, *56*, 2420.

[9] Y. Yang, D. M. Davies, Y. Yin, O. Borodin, J. Z. Lee, C. Fang, E. S. Sablina, X. Wang, C. S. Rustomji, Y. S. Meng, *Joule* **2019**, *3*, 1986.

[10] A. Ahmadiparidari, R. E. Warburton, L. Majidi, M. Asadi, A. Chamaani, J. R. Jokisaari, S. Rastegar, Z. Hemmat, B. Sayahpour, R. S. Assary, B. Narayanan, P. Abbasi, P. C. Redfern, A. Ngo, M. Vörös, J. Greeley, R. Klie, L. A. Curtiss, A. Salehi-khojin, *Adv. Mater.* **2019**, *31*, 1902518.

[11] X. Li, J. Zhou, J. Zhang, M. Li, J. Cheng, F. Zhang, Y. Li, X. Mu, J. Lu, B. Wang, *Adv. Mater.* **2019**, *31*, 1903852.

[12] L. Ye, M. Liao, T. Zhao, H. Sun, Y. Zhao, X. Sun, B. Wang, H. Peng, *Angew. Chem. Int. Ed.* **2019**, *58*, 17054.

[13] J. Ma, F. Meng, Y. Yu, D. Liu, J. Yan, Y. Zhang, X. Zhang, Q. Jiang, *Nat. Chem.* **2018**, *11*, 64.

[14] S. A. Freunberger, Y. Chen, N. E. Drewett, L. J. Hardwick, F. Bardø, P. G. Bruce, *Angew. Chem. Int. Ed.* **2011**, *50*, 8609.

[15] Z. Huang, H. Zeng, M. Xie, X. Lin, Z. Huang, Y. Shen, Y. Huang, *Angew. Chem. Int. Ed.* **2019**, *58*, 2345.

[16] Y. Chen, S. A. Freunberger, Z. Peng, F. Bardé, P. G. Bruce, *J. Am. Chem. Soc.* **2012**, *124*, 7952.

[17] W. Wesley, V. Giordani, J. Uddin, V. S. Bryantsev, G. V. Chase, D. Addison, *J. Am. Chem. Soc.* **2013**, *135*, 2076.

[18] Z. Tang, Y. Mao, J. Xie, G. Cao, D. Zhuang, G. Zhang, W. Zheng, X. Zhao, *ACS Appl. Mater. Interfaces* **2018**, *10*, 25925.

[19] B. Liu, W. Xu, J. Zheng, P. Yan, E. D. Walter, N. G. Isern, M. E. Bowden, M. H. Engelhard, S. T. Kim, J. Read, B. D. Adams, X. Li, J. Cho, C. Wang, J.-G. Zhang, *ACS Energy Lett.* **2017**, *2*, 2525.

[20] H. Song, S. Wang, X. Song, J. Wang, K. Jiang, S. Huang, M. Han, J. Xu, P. He, K. Chen, H. Zhou, *Energy Environ. Sci.* **2020**.

[21] Z. Pei, Z. Yuan, C. Wang, J. Fei, L. Wei, J. Chen, C. Wang, R. Qi, Z. Liu, Y. Chen, *Angew. Chem. Int. Ed.* **2020**, *59*, 4793.